


Article

2D/2D Heterojunction of TiO₂ Nanoparticles and Ultrathin G-C₃N₄ Nanosheets for Efficient Photocatalytic Hydrogen Evolution

Ruifeng Du ^{1,2}, Baoying Li ^{3,*}, Xu Han ⁴, Ke Xiao ^{1,2}, Xiang Wang ^{1,2}, Chaoqi Zhang ^{1,2}, Jordi Arbiol ^{4,5} 
and Andreu Cabot ^{1,5,*}

¹ Catalonia Energy Research Institute—IREC, Sant Adrià de Besòs, 08930 Barcelona, Spain; ruifengdu@irec.cat (R.D.); kexiao@irec.cat (K.X.); xwang@irec.cat (X.W.); czhang@irec.cat (C.Z.)

² Departament d'Enginyeria Electrònica i Biomèdica, Universitat de Barcelona, 08028 Barcelona, Spain

³ Shandong Provincial Key Laboratory of Molecular Engineering, State Key Laboratory of Biobased Material and Green Papermaking, School of Chemistry and Chemical Engineering, Qilu University of Technology, Shandong Academy of Sciences, Jinan 250353, China

⁴ Catalan Institute of Nanoscience and Nanotechnology (ICN2), CSIC and BIST, Campus UAB, Bellaterra, 08193 Barcelona, Spain; xuhan@irec.cat (X.H.); arbiol@icrea.cat (J.A.)

⁵ ICREA, Pg. Lluís Companys 23, 08010 Barcelona, Spain

* Correspondence: libaoying@qlu.edu.cn (B.L.); acabot@irec.cat (A.C.)

Abstract: Photocatalytic hydrogen evolution is considered one of the promising routes to solve the energy and environmental crises. However, developing efficient and low-cost photocatalysts remains an unsolved challenge. In this work, ultrathin 2D g-C₃N₄ nanosheets are coupled with flat TiO₂ nanoparticles as face-to-face 2D/2D heterojunction photocatalysts through a simple electrostatic self-assembly method. Compared with g-C₃N₄ and pure TiO₂ nanosheets, 2D/2D TiO₂/g-C₃N₄ heterojunctions exhibit effective charge separation and transport properties that translate into outstanding photocatalytic performances. With the optimized heterostructure composition, stable hydrogen evolution activities are threefold and fourfold higher than those of pure TiO₂, and g-C₃N₄ are consistently obtained. Benefiting from the favorable 2D/2D heterojunction structure, the TiO₂/g-C₃N₄ photocatalyst yields H₂ evolution rates up to 3875 μmol·g⁻¹·h⁻¹ with an AQE of 7.16% at 380 nm.

Keywords: hydrogen evolution; 2D/2D heterojunction; charge separation



Citation: Du, R.; Li, B.; Han, X.; Xiao, K.; Wang, X.; Zhang, C.; Arbiol, J.; Cabot, A. 2D/2D Heterojunction of TiO₂ Nanoparticles and Ultrathin G-C₃N₄ Nanosheets for Efficient Photocatalytic Hydrogen Evolution. *Nanomaterials* **2022**, *12*, 1557. <https://doi.org/10.3390/nano12091557>

Academic Editor: Nikos Tagmatarchis

Received: 8 April 2022

Accepted: 28 April 2022

Published: 4 May 2022

Publisher's Note: MDPI stays neutral with regard to jurisdictional claims in published maps and institutional affiliations.



Copyright: © 2022 by the authors. Licensee MDPI, Basel, Switzerland. This article is an open access article distributed under the terms and conditions of the Creative Commons Attribution (CC BY) license (<https://creativecommons.org/licenses/by/4.0/>).

1. Introduction

Owing to the abundance of low-cost solar energy, the numerous uses of hydrogen and its advantages as an energy carrier, the photocatalytic generation of hydrogen is a highly appealing process [1,2]. However, the cost-effective photogeneration of hydrogen requires high activity and stable photocatalysts, development of which has been a long-standing goal. Over the past decades, numerous semiconductors have been tested as photocatalysts for hydrogen evolution. Among them, titanium dioxide (TiO₂) has received special attention owing to its stability, high abundance, low toxicity, being the earliest to be discovered and becoming the first to be industrialized [3]. Nevertheless, due to its wide bandgap and relatively fast charge recombination rate, its applicability has been strongly limited. Numerous strategies have been proposed to improve the photocatalytic performance of TiO₂, facilitating charge separation and promoting efficiency and activity, [4–7] including the control of its particle facets and morphology [8–11], its modification with cocatalysts [12–15] and its coupling with other semiconductors to form heterostructures [16–24].

Graphite carbonitride (g-C₃N₄) with a layered structure similar to graphite, high chemical stability and low cost has received increasing interest in recent years [25–27]. In particular, as a polymeric semiconductor, g-C₃N₄ has been recently reported as a promising candidate photocatalyst due to its unique structure and electronic characteristics, with a

2.7 eV bandgap that allows absorbing part of the visible spectrum [28,29]. Additionally, two-dimensional (2D) g-C₃N₄ nanosheets, benefiting from a huge specific surface area and a suitable band structure, have shown especially interesting properties and offer an excellent platform to produce heterojunctions with other semiconductors [30–33].

Recently, 2D/2D heterojunctions have been demonstrated to provide great advantages to improve charge separation [34,35]. 2D/2D heterojunctions simultaneously maximize the interface and surface areas, i.e., the charge transfer between the two materials and the interaction with the media, which can potentially improve photocatalytic activities.

In the present work, we target improving photocatalytic hydrogen production using 2D/2D heterojunctions. In this direction, we report the first synthesis of 2D/2D TiO₂/g-C₃N₄ heterostructures. Such composite materials are produced from the electrostatic assembly of 2D anatase TiO₂ flat nanoparticles synthesized through a simple colloidal method with 2D ultrathin g-C₃N₄. The produced heterostructures are tested as photocatalysts for hydrogen evolution under simulated solar light irradiation. The excellent hydrogen evolution performance obtained after optimizing the weight contents of TiO₂ and g-C₃N₄ within 2D/2D heterojunction are rationalized using photoluminescence, photocurrent and impedance spectroscopy analysis.

2. Experiment

Synthesis of bulk g-C₃N₄ (bCN) and ultrathin g-C₃N₄ (uCN): Bulk g-C₃N₄ powder was synthesized by thermal polymerization of urea. Briefly, 10 g of urea (99%, Acros Organics) was placed into a ceramic crucible. The crucible was covered and heated to 550 °C at a ramp rate of 2 °C min⁻¹ for 4 h under air atmosphere. After cooling to room temperature, the resulting light-yellow solid was ground with the mortar to obtain the bulk g-C₃N₄ powder. To obtain ultrathin g-C₃N₄ (uCN), bulk g-C₃N₄ (2.0 g) was placed in a covered ceramic crucible, and it was heated to 520 °C with a ramp rate of 5 °C min⁻¹ for 2 h under air atmosphere to obtain a light-yellow powder.

Synthesis of TiO₂ nanosheets: Titanium dioxide nanoparticles were prepared using a colloidal method. All the syntheses were performed using standard airless techniques [36,37]. Typically, 10 mL of oleylamine (OAm, 80–90%, Acros Organics, Geel, Belgium), 10 mL of octadecene (ODE, 90%, Sigma-Aldrich, Burlington, MA, USA) and 1 mL of oleic acid (OAc, 90%, Sigma-Aldrich, Burlington, MA, USA) were loaded in a three-neck flask and degassed under vacuum at 120 °C for 1 h while being strongly stirred using a magnetic bar. Then, 300 mg of TiF₄ (99%, Sigma, Burlington, MA, USA) was added in a mixed solution of 2 mL OAm, 3 mL OAc and 6 mL ODE and sonicated for 0.5 h to prepare a precursor solution. Subsequently, under nitrogen atmosphere, 10 mL of the precursor solution were slowly added to the reaction flask, which was then heated to 290 °C at a rate of 5 °C min⁻¹ and maintained for 1 h. The solid product was centrifuged and washed with acetone and hexane three times. The particles were finally dispersed in hexane at a concentration of 10 mg/mL.

Ligand removal from TiO₂ nanoparticles: In a typical process, 10 mL of a TiO₂ dispersion in hexane (2 mg/mL) was combined with 10 mL acetonitrile to form a two-phase mixture. Then, 1 mL of a HBF₄ solution (48%, Sigma-Aldrich, Burlington, MA, USA) was added. The resulting solution was sonicated until the particles transferred from the upper to the bottom layer. The surface-modified particles were washed with ethanol and a 1 mol/L sodium hydroxide (85%, Sigma-Aldrich, Burlington, MA, USA) aqueous solution three times to remove the residual fluoride ions and ligands. The particles were then washed with water to adjust the PH close to neutral. Finally, the particles were dispersed in 10 mL of water with a small amount of DMF.

Synthesis of 2D/2D TiO₂/ultrathin g-C₃N₄ (TiO₂/uCN) composite: TiO₂/uCN heterojunctions were produced by an electrostatic self-assembly method. Briefly, 20 mg of as prepared ultrathin g-C₃N₄ was dissolved in 10 mL of ultrapure water and sonicated for 1 h. The solution was then mixed with an ethanol solution of ligand-removed TiO₂ nanoparticles with a weight ratio of 1:2, 1:1 and 2:1. The mixed solution was stirred for

24 h after 1 h of sonication. The obtained composite was collected by centrifuging, it was washed with ethanol 2 times, and it was finally dried at 60 °C for 12 h. The collected materials were named T₁/uCN₂, T₁/uCN₁ and T₂/uCN₁ based on the different TiO₂/ultrathin g-C₃N₄ weight ratios. TiO₂/bulk g-C₃N₄ (T/bCN) samples were prepared using the same procedure. For photocatalytic measurements, 1 wt% of Pt was loaded on the surface of the photocatalysts by a photoreduction method.

Photocatalytic Hydrogen Evolution Procedure

The photocatalytic hydrogen evolution experiments were carried out in a Perfect Light Labsolar-III (AG) photoreactor (Pyrex glass) connected to a closed-loop gas circulation system. In a typical experiment, 20 mg photocatalyst was dispersed in 100 mL aqueous solution containing 10 mL methanol and 1 wt% Pt cocatalyst (40 μ L 25.625 mmol/L H₂PtCl₆ aqueous solution). The mixed solution was bubbled with N₂ for 30 min to ensure anaerobic state and illuminated 30 min with UV light before simulated solar light irradiation to ensure the complete loading of Pt. The incident light was provided by a 300 W Xe lamp with an AM 1.5 filter, and the reaction conditions were kept at room temperature. The resulting gas was analyzed by a Labsolar-III (AG) gas chromatograph equipped with a thermal conductivity detector, with high-purity argon as the carrier gas.

3. Result and Discussion

TiO₂/g-C₃N₄ heterostructures were obtained by the electrostatic assembly of TiO₂ nanoparticles and ultrathin g-C₃N₄ nanosheets (Figure 1, see Experimental section for details). Colloidal TiO₂ nanoparticles were produced in the presence of OAm and OAc using TiF₄ as the Ti precursor. As shown in Figure 2a, low-resolution TEM images exhibited the TiO₂ particles to have a flat square morphology with a side length of 30–50 nm and a thickness of about 5–10 nm. g-C₃N₄ nanosheets were produced by the thermal etching of bulk g-C₃N₄. As observed by scanning electron microscopy (SEM, Figure S1a,b) and transmission electron microscopy (TEM, Figure 2b) characterization, bCN and uCN displayed significantly different morphologies. The uCN showed a thin nanosheet-based structure pointing at the occurrence of a layer etching during the thermal process. Figure S1c displays the nitrogen adsorption–desorption isotherms of bCN and uCN, which further proved uCN (85.7 m²/g) to be characterized by a larger specific surface area than bCN (46.3 m²/g).

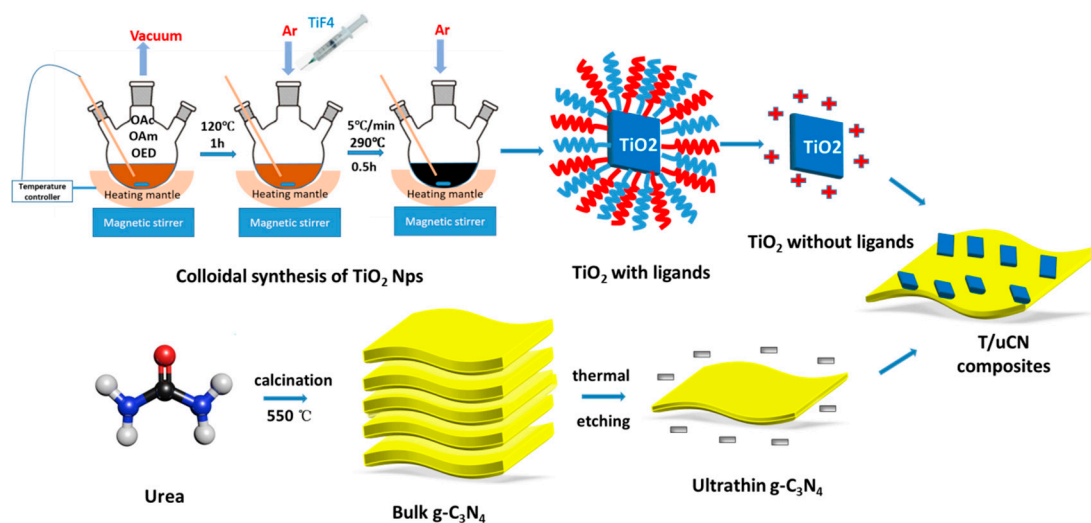


Figure 1. Schematic illustration of the process used to produce 2D/2D TiO₂/uCN composite.

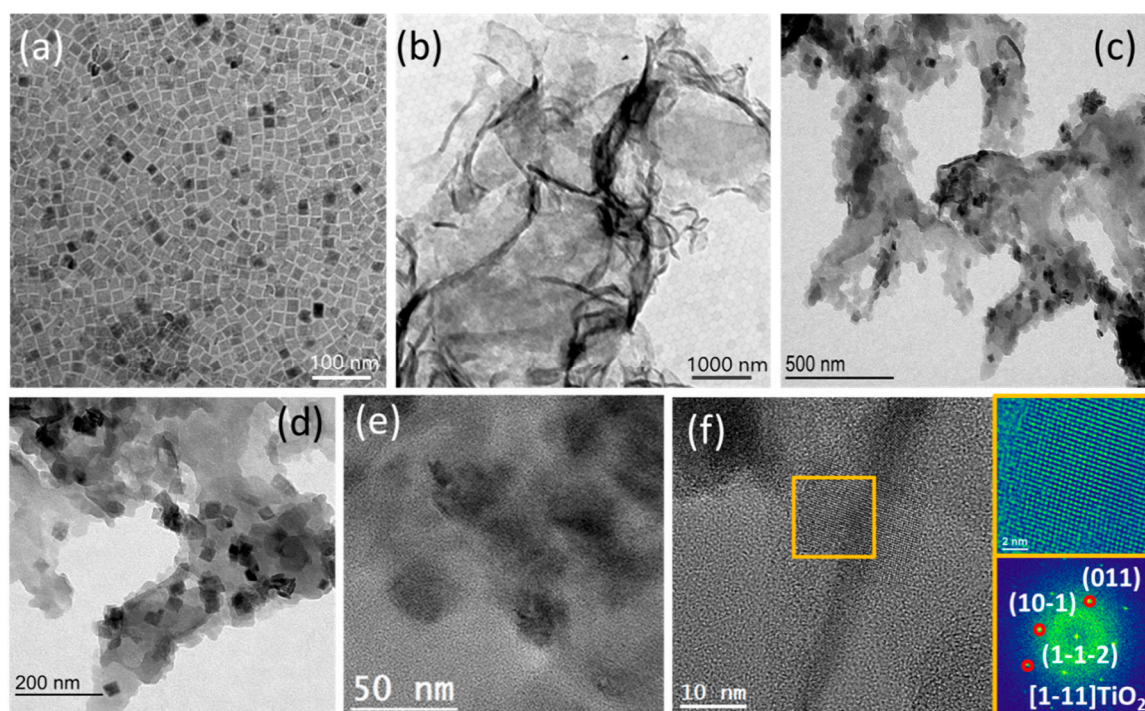


Figure 2. Representative TEM images of (a) TiO₂ nanoparticles; (b) g-C₃N₄ nanosheets and T₁/uCN₁ composite with representative (c) low and (d) high magnification. (e,f) HRTEM images of T₁/uCN₁. A magnified detail (top right) of the orange squared region in the HRTEM image and its corresponding indexed power spectrum (bottom right) is shown, revealing the TiO₂ anatase phase (space group = I4₁/amd) with $a = b = 3.7840 \text{ \AA}$, and $c = 9.5000 \text{ \AA}$. TiO₂ lattice fringe distances were measured to be 0.233 nm, 0.352 nm and 0.348 nm at 41.30° and 139.38°, which could be interpreted as the anatase TiO₂ phase, visualized along its [1-11] zone axis.

To positively charge the surface of the TiO₂ particles, enable their dispersion in an aqueous solution and promote charge transfer with the media; the organic ligands attached to the particle surface were removed using HBF₄ (Figure S2). As observed by zeta-potential analysis, while the g-C₃N₄ nanosheets were negatively charged ($V = -33.8 \text{ mV}$), after ligands removal the TiO₂ particles were positively charged ($V = +18.6 \text{ mV}$), which enabled the electrostatic self-assembly of the two components [38]. Indeed, when combining solutions of the two types of material, a light-yellow precipitate was formed. The precipitate was composed of large uCN nanosheets containing numerous nanoparticles attached to their surface. TEM analyses showed these nanoparticles lie flat on the surface of uCN, forming 2D/2D heterostructures (Figure 2c,d). High resolution TEM (HRTEM) further confirmed these nanoparticles are TiO₂ with good crystallinity (Figure 2e,f).

SEM-EDS elemental maps (Figure S4) displayed a homogeneous distribution of C, N, O and Ti, demonstrating a uniform distribution of TiO₂ particles on the uCN surface at the microscale. On the other hand, quantitative EDX analyses showed the TiO₂:CN weight ratio to be close to that of the nominal combination of each phase: TiO₂:CN = 0.47 for T₁/uCN₂; TiO₂:CN = 1.1 for T₁/uCN₁ and TiO₂:CN = 1.9 for T₂/uCN₁, obtained from mixing 1:2, 1:1 and 2:1 mass ratios of particles, respectively (Figures S5–S7).

Figure 3a displays the X-ray diffraction (XRD) patterns of bCN, uCN, TiO₂ and T/uCN samples. The XRD peaks at 25.2° (101), 38.0° (004), 47.7° (200) and 54.8° (211) are associated with the anatase TiO₂ phase (JCPDS No. 21-1272) [39]. Additionally, the characteristic diffraction peaks at 13.1° and 27.4° correspond to the (002) and (100) planes of g-C₃N₄ (JCPDS No. 87-1526) [40]. The characteristic diffraction peaks of both TiO₂ and g-C₃N₄ can be observed in all the composites samples, confirming the coexistence of anatase TiO₂ and g-C₃N₄.

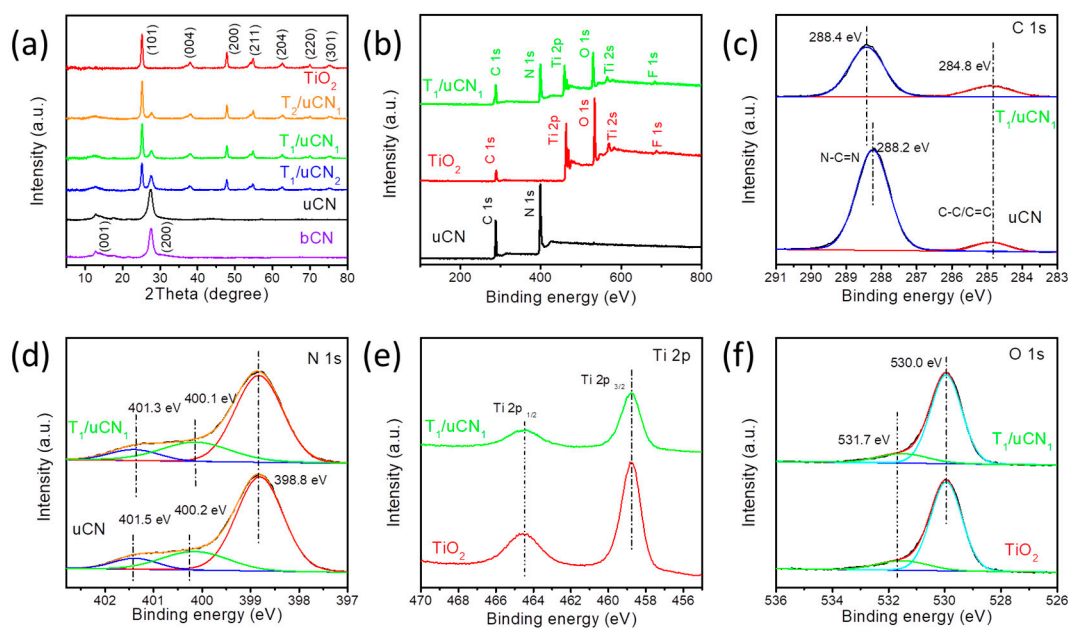


Figure 3. (a) XRD patterns of TiO_2 , uCN and T/uCN. (b) XPS survey spectrum of TiO_2 , uCN and T/uCN; high-resolution XPS spectra at the regions (c) C 1s, (d) N 1s, (e) Ti 2p and (f) O 1s.

The X-ray photoelectron spectroscopy spectra of TiO_2 , uCN and T/uCN are displayed in Figure 3b–f. As observed from the survey XPS spectrum, besides Ti, C, O and N, a residual amount of F from the TiF_4 precursor used to prepare the TiO_2 particles was also present in the final material (Figure 3b). The high-resolution C 1s XPS spectrum of uCN showed two main contributions at 288.2 eV and 284.8 eV, which were assigned to C-(N3) and C–C/C=C, respectively (Figure 3c). Compared with pure uCN, the peak for C-(N3) of the T_1/uCN_1 sample was slightly shifted to 288.2 eV. The high-resolution N 1s XPS spectra were deconvoluted using three contributions at binding energies of 398.1 eV, 499.4 eV and 400.5 eV for uCN and 398.1 eV, 499.6 eV and 400.7 eV for T/uCN (Figure 3d). These three contributions were assigned to N-(C₂), N-(C₃) and N-H_x groups of the heptazine framework. The small shifts detected for C and some of the N components might be related to a certain degree of charge between the TiO_2 and the CN phases. Figure 3e displays the high-resolution Ti 2p XPS spectra of TiO_2 and T/uCN. Both samples show two strong peaks at approximately 458.7 and 464.5 eV, which are assigned to the Ti 2p_{3/2} and Ti 2p_{1/2} levels of Ti within a TiO_2 environment. The high-resolution O 1s XPS spectra of TiO_2 and T/uCN were fitted with two peaks at 530.4 eV and 531.8 eV, which were associated with oxygen within the TiO_2 lattice and oxygen-containing surface adsorption groups such as surface hydroxyl, respectively (Figure 3f).

The UV-vis spectra showed the UV absorption edge of TiO_2 particles and uCN nanosheets at about 390 nm and 445 nm, respectively (Figure 4a). T/uCN composites showed a similar onset absorption edge as uCN but an increased absorption below 400 nm related to the presence of the TiO_2 component. All TiO_2 and T/uCN samples presented a small absorption in the range 500–800 nm related to a small amount of F ion doping. According to the Kubelk–Munk function, the band gaps of TiO_2 , uCN and T_1/uCN_1 samples were calculated at about 3.02 eV, 2.62 eV and 2.65 eV, respectively (Figure 4b).

According to Mott–Schottky analyses (Figure 4c,d and Figure S3), the flat band potentials of TiO_2 and uCN were -0.36 V and -0.86 V vs. the normal hydrogen electrode (NHE). The valence band (VB) XPS spectra of TiO_2 and uCN showed the valence band maximum (VBM) to be located at 2.89 eV and 2.46 eV from the Fermi level, respectively. Since the flat band potentials are approximately equal to the Fermi level [41,42], the VBM was located at 2.53 eV and 1.60 eV with respect to the NHE for TiO_2 and uCN, respectively. Then, taking into account the calculated band gaps ($E_g = E_{vb} - E_{cb}$) [43], the conduction band minimum (CBM) was located at 0.49 and -1.02 for TiO_2 and uCN, respectively. Figure 4f displays

the energy-level diagram calculated for TiO₂ and uCN samples. According to this scheme, when combining uCN with TiO₂, a type II heterojunction is formed, involving electron transfer from the uCN to the TiO₂ particles. Besides, it is predicted that within such heterostructure, photogenerated electrons move toward the TiO₂ phase and photogenerated holes toward the uCN, respectively.

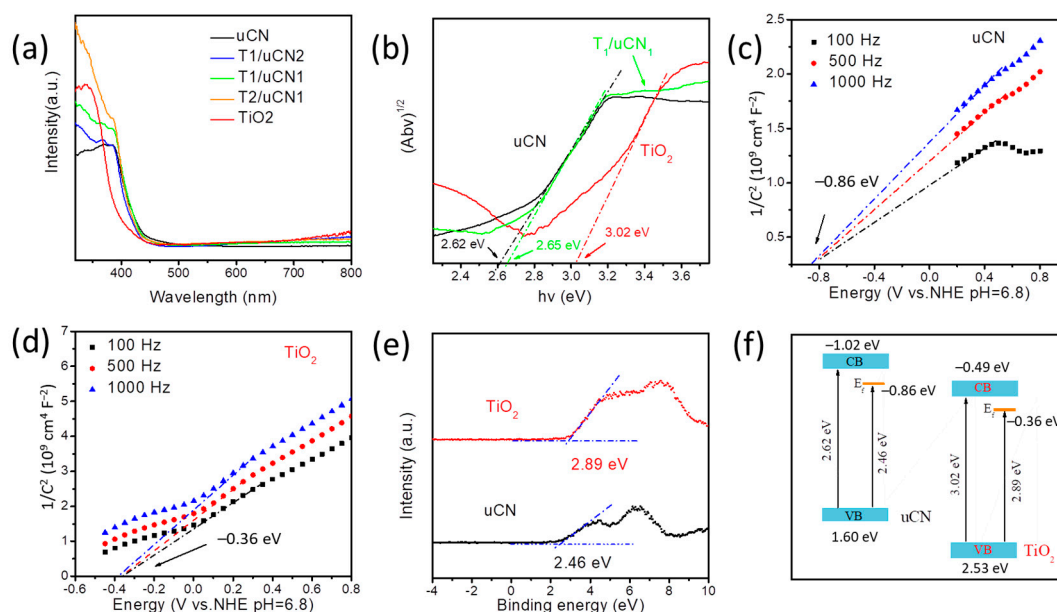


Figure 4. (a) UV-vis absorption spectra. (b) Kubelka–Munk-transformed function of TiO₂, uCN and T₁/uCN₁. (c,d) Mott–Schottky plots of uCN (c) and TiO₂ (d). (e) Valence band XPS spectrum of TiO₂ and uCN. (f) Diagram of the band structure of TiO₂ and uCN.

To analyze the photocatalytic activity towards hydrogen generation, all the samples were loaded with 1 wt% platinum as cocatalyst. Figure 5 displays the photocatalytic hydrogen generation from bCN, uCN, TiO₂ and TiO₂/uCN composites for 4 h under simulated solar light and using methanol as a sacrificial agent. Figures S8 and S9 and Table S2 show the chromatogram plots and the linear fitting of the standard hydrogen curve for gas chromatography, which show our measurement error is less than 0.2%.

For TiO₂, a high hydrogen evolution rate (HER) up to 1449 $\mu\text{mol}\cdot\text{g}^{-1}\cdot\text{h}^{-1}$ was obtained. Additionally, a notable HER was also obtained from uCN (801 $\mu\text{mol}\cdot\text{g}^{-1}\cdot\text{h}^{-1}$), well above that of bCN (599 $\mu\text{mol}\cdot\text{g}^{-1}\cdot\text{h}^{-1}$), which is consistent with the larger surface area provided by the thin-layered structure of uCN. All the TiO₂/uCN composites displayed a significant HER improvement with respect to pure TiO₂ or uCN. The highest HERs were obtained with the TiO₂/uCN composites having a 1:1 weight ratio of the two components, reaching a HER of 3875 $\mu\text{mol}\cdot\text{g}^{-1}\cdot\text{h}^{-1}$, which is 2.7 and 4.8 times higher than that of TiO₂ and uCN, respectively. The observed synergistic effect obtained when mixing both materials is related to the transfer and thus separation of photogenerated carriers at the 2D/2D heterojunctions, which prevents their recombination. Table S3 provides a comparison of the activity obtained here with those of previous published works, demonstrating the outstanding activity provided by the 2D/2D TiO₂/uCN heterojunction.

As a reference, we also measured the HER of TiO₂/bCN composites with the optimized weight ratio 1:1 (T₁/bCN₁). As observed in Figure 5c and Figure S7, the HER of T₁/bCN₁ also showed an obvious improvement with respect to that of pure TiO₂ and bCN, but the highest HER values were well below those of 2D/2D T/uCN heterojunctions having extended surface and interface areas.

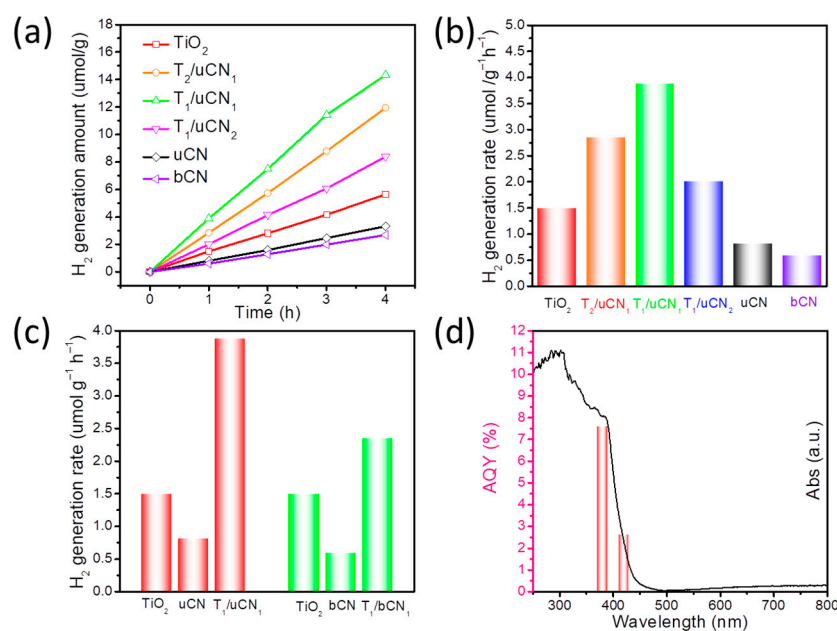


Figure 5. (a) Photocatalytic hydrogen generation on bCN, TiO₂ and T/uCN samples during four hours under simulated solar light illumination. (b) Photocatalytic hydrogen peroxide generation rate of bCN, TiO₂ and T/uCN samples. (c) H₂ production rate contrast between T₁/uCN₁ and T₁/bCN₁. (d) Wavelength-dependent AQY of T₁/uCN₁.

The apparent quantum yield (AQY) of the process was evaluated under 380 nm (4.51 mW·cm⁻²) and 420 nm (12.14 mW·cm⁻²) irradiation (Table S4, see details in the SI). For T₁/uCN₁, the AQY at 380 nm and 420 nm was estimated at 7.61% and 2.64%, respectively, which is consistent with UV-vis spectroscopy results (Figure 5d).

Figure 6a displays the positive photocurrents measured from uCN, TiO₂ and TiO₂/uCN samples under simulated solar irradiation. All the composite T/uCN, electrodes displayed significantly higher photocurrents than pure TiO₂ and uCN, especially the T₁/uCN₁ electrode that showed the highest photocurrents, fourfold higher than those of uCN and TiO₂. This result further confirms an improvement of the charge separation/transport with the formation of the 2D/2D heterojunction.

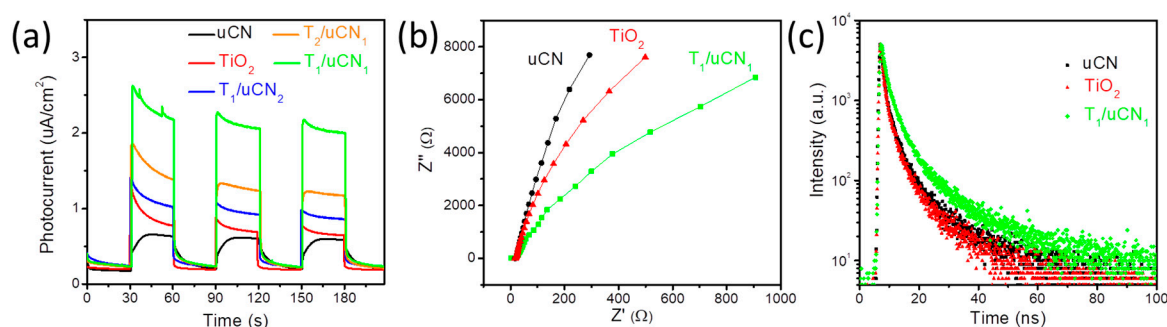


Figure 6. (a) Photocurrent response curves of bCN, TiO₂ and T/uCN samples; (b) electrochemical impedance spectroscopy (EIS) Nyquist plots of bCN, TiO₂ and T₁/uCN₁ sample; (c) TRPL decay of bCN, TiO₂ and T/uCN samples.

Electrochemical impedance spectroscopy (EIS) was further employed to identify the charge transport dynamics. Figure 6b displays the Nyquist plot of the impedance spectra of TiO₂, uCN and T₁/uCN₁. Consistent with previous results, the T₁/uCN₁ electrode presented a much smaller arc radius than the other two samples, confirming a much lower charge transfer resistance with the formation of the 2D/2D TiO₂/uCN heterojunction [44].

A strong photoluminescence (PL) peak was obtained under 370 nm light excitation from the uCN sample at about 455 nm, which is ascribed to the radiative band-to-band recombination of photogenerated charge carriers. When incorporating increasing amounts of TiO₂, the PL intensity of T/uCN was progressively quenched (Figure S10). Additional time-resolved PL (TRPL) spectra under 365 nm light excitation (Figure 6c) allowed calculating significantly longer PL lifetimes (4.72 ns) for T₁/uCN₁ samples than for TiO₂ (3.15 ns) and uCN (3.51 ns), which points at an effective separation of photogenerated charge carriers within the TiO₂/uCN heterostructures [45].

Based on the above results, the photocatalytic mechanism displayed in Figure 7 is proposed for hydrogen generation in T/uCN heterojunction photocatalysts. While both TiO₂ and uCN can generate electrons and holes under simulated solar light irradiation, the photogenerated electron–hole pairs in pure TiO₂ and uCN rapidly recombine, resulting in moderate HERs. Through the formation of a 2D/2D T/uCN heterostructure, the photogenerated electrons remain or are transferred to the TiO₂ CB because the TiO₂ CBM is located 0.53 eV below that of CN. Similarly, photogenerated holes remain or are driven to the uCN VB, which is located 0.93 eV above that of TiO₂. Electrons at the TiO₂ CB migrate to the platinum, which has a larger work function, thus a lower Fermi level, from where they are transferred to adsorbed H⁺ to produce H₂. On the other hand, holes react with sacrificial methanol at the CN surface. Consequently, the photocatalytic hydrogen evolution process using sacrificial methanol can be described as follows:

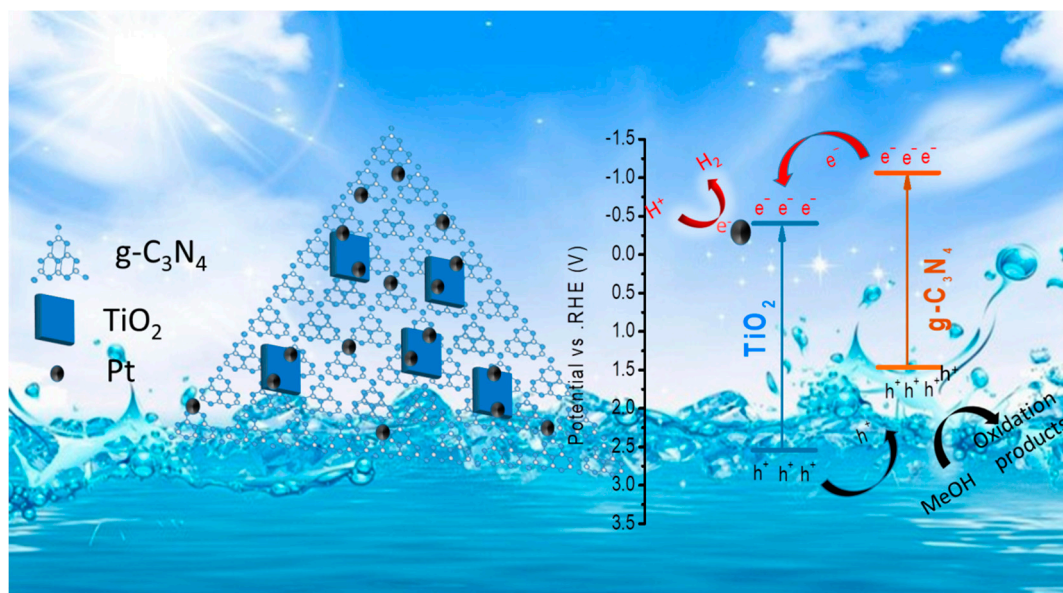
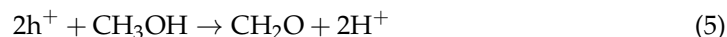
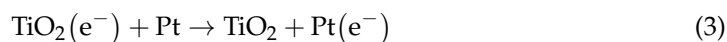
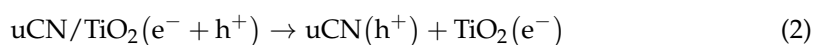
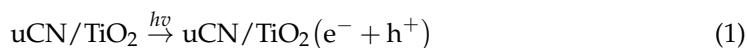


Figure 7. Schematic diagram of photocatalytic hydrogen production over T/uCN photocatalyst.

Finally, the stability of the T₁/uCN₁ photocatalyst in hydrogen evolution conditions under simulated solar light irradiation was measured through five four-hour cycles. As shown in Figure S11a, after this 20 h of reaction, the photocatalytic performance was hardly reduced, proving the excellent stability and reusability of the T₁/uCN₁ photocatalyst. Additionally, as displayed in Figure S11b,c, SEM and XRD analysis of the catalyst after 20 h

photocatalytic hydrogen generation reaction demonstrated the morphology and crystallographic structure of the material to be stable under photocatalytic reaction conditions.

4. Conclusions

In summary, we detailed the synthesis of 2D/2D T/uCN heterojunctions from ultrathin g-C₃N₄ (uCN) and colloidal TiO₂ nanosheets through an electrostatic self-assembly approach. The highest hydrogen generation rate was achieved from T/uCN composites with a 1:1 mass ratio of the two components. The photocatalytic performance for H₂ production was increased in the following order: bCN < uCN < TiO₂ < T₁/uCN₂ < T₂/uCN₁ < T₁/uCN₁. The enhanced performance was attributed to the unique 2D/2D type II heterojunction architecture that simultaneously maximized the surface area to interact with the media and the interface between the two materials. The face-to-face interfacial contact between ultrathin layers of g-C₃N₄ and the faceted TiO₂ provided fast separation of photogenerated charges inside the composites, reducing recombination and thus increasing the apparent quantum yield.

Supplementary Materials: The following supporting information can be downloaded at: <https://www.mdpi.com/article/10.3390/nano12091557/s1>, Figure S1: SEM image of (a) bulk g-C₃N₄ and (b) ultrathin g-C₃N₄, (c) N₂ adsorption-desorption isotherms of bCN and uCN; Figure S2: FTIR spectra of OAC, OLMA and TiO₂ before and after ligands remove; Figure S3: Zeta potential distribution spectrum of TiO₂ after ligands removal (a) and uCN (b); Figure S4: SEM image and EDS compositional maps of a T₁/uCN₁ composite; Figure S5: SEM image of T₁/uCN₂ and corresponding EDS spectrum; Figure S6: SEM image of T₁/uCN₂ and corresponding EDS spectrum; Figure S7: SEM image of T₁/uCN₂ and corresponding EDS spectrum; Figure S8: Chromatogram plots for 0.5 mL of standard hydrogen injected every half hour; Table S1: Gas Chromatography Peak Processing Data based on figure S8; Figure S9: Standard hydrogen curve for gas chromatography; Table S2: Exponential decay-fitted parameters of fluorescence lifetime of uCN, TiO₂ and T₁/uCN₁; Figure S10: Photocatalytic hydrogen generation amount on bCN, TiO₂ and T₁/bCN₁ during 4 h under simulated solar light irradiation; Table S3: Photocatalytic hydrogen production about TiO₂/g-C₃N₄ based catalysts; Table S4: The AQE values with different incident light wavelengths for T₁/uCN₁; Figure S11: (a) Stability cycles of the T₁/uCN₁ for H₂ evolution under simulated solar light irradiation; (b) TEM image of T₁/uCN₁ after 20 h photocatalytic H₂ evolution reaction and (c) XRD pattern of T₁/uCN₁ before and after 20 h photocatalytic H₂O₂ evolution reaction.

Author Contributions: In this work, R.D. designed the experiment and the nanocomposites, prepared all the materials and conducted XRD, SEM, ZEM-EDS, TEM characterization, photoelectrochemical measurements and wrote the first draft of the manuscript. B.L. conducted the photocatalytic hydrogen evolution test and TRPL test. K.X., C.Z. and X.W. significantly contributed to the result discussion. X.H. and J.A. participated in high-resolution TEM characterization. A.C. conceived and guided the project and supervised the work. The manuscript was corrected and improved by all authors. All authors have read and agreed to the published version of the manuscript.

Funding: R.D.: K.X., X.H., X.W. and C.Z. thank the China Scholarship Council for the scholarship support. IREC and ICN2 acknowledge funding from Generalitat de Catalunya, projects 2017 SGR 1246 and 2017 SGR 327, respectively. The authors thank the support from the project NANOGEN (PID2020-116093RB-C43), funded by MCIN/AEI/10.13039/501100011033/ and the project COMBENERGY (PID2019-105490RB-C32) from the Spanish Ministerio de Ciencia e Innovación. ICN2 is supported by the Severo Ochoa program from Spanish MINECO (Grant No. SEV-2017-0706) and is funded by the CERCAProgramme / Generalitat de Catalunya. Baoying Li greatly appreciates the financial support from the National Natural Science Foundation of China (Nos. 22171154 & 21801144), the Youth Innovative Talents Recruitment and the Cultivation Program of Shandong Higher Education. This study was supported by MCIN with funding from the European Union NextGenerationEU (PRTR-C17.I1), Generalitat de Catalunya and by “ERDF A way of making Europe” by the “European Union”.

Institutional Review Board Statement: Not applicable.

Informed Consent Statement: Not applicable.

Data Availability Statement: The data are available on reasonable request from the corresponding authors.

Conflicts of Interest: The authors declare no conflict of interest.

References

1. Campos-Martin, J.M.; Blanco-Brieva, G.; Fierro, J.L.G. Hydrogen peroxide synthesis: An outlook beyond the anthraquinone process. *Angew. Chem. Int. Ed.* **2006**, *45*, 6962–6984. [[CrossRef](#)] [[PubMed](#)]
2. Xiang, Q.; Cheng, B.; Yu, J. Hierarchical porous CdS nanosheet-assembled flowers with enhanced visible-light photocatalytic H₂-production performance. *Appl. Catal. B Environ.* **2013**, *138*, 299–303. [[CrossRef](#)]
3. Fujishima, A.; Honda, K. Electrochemical photolysis of water at a semiconductor electrode. *Nature* **1972**, *238*, 37–38. [[CrossRef](#)] [[PubMed](#)]
4. Zhang, J.; Xu, Q.; Feng, Z.; Li, M.; Li, C. Importance of the relationship between surface phases and photocatalytic activity of TiO₂. *Angew. Chem.* **2008**, *120*, 1790–1793. [[CrossRef](#)]
5. Irie, H.; Watanabe, Y.; Hashimoto, K. Carbon-doped anatase TiO₂ powders as a visible-light sensitive photocatalyst. *Chem. Lett.* **2003**, *32*, 772–773. [[CrossRef](#)]
6. Zhang, Y.; Tang, Z.-R.; Fu, X.; Xu, Y.-J. TiO₂–graphene nanocomposites for gas-phase photocatalytic degradation of volatile aromatic pollutant: Is TiO₂–graphene truly different from other TiO₂–carbon composite materials? *ACS Nano* **2010**, *4*, 7303–7314. [[CrossRef](#)] [[PubMed](#)]
7. Thompson, T.L.; Yates, J.T. Surface science studies of the photoactivation of TiO₂ new photochemical processes. *Chem. Rev.* **2006**, *106*, 4428–4453. [[CrossRef](#)]
8. Hamad, S.; Catlow, C.R.A.; Woodley, S.M.; Lago, S.; Mejias, J.A. Structure and stability of small TiO₂ nanoparticles. *J. Phys. Chem. B* **2005**, *109*, 15741–15748. [[CrossRef](#)]
9. Sang, L.; Zhao, Y.; Burda, C. TiO₂ nanoparticles as functional building blocks. *Chem. Rev.* **2014**, *114*, 9283–9318. [[CrossRef](#)]
10. Chen, J.S.; Lou, X.W. Anatase TiO₂ nanosheet: An ideal host structure for fast and efficient lithium insertion/extraction. *Electrochem. Commun.* **2009**, *11*, 2332–2335. [[CrossRef](#)]
11. Zhang, Y.X.; Li, G.H.; Jin, Y.X.; Zhang, Y.; Zhang, J.; Zhang, L.D. Hydrothermal synthesis and photoluminescence of TiO₂ nanowires. *Chem. Phys. Lett.* **2002**, *365*, 300–304. [[CrossRef](#)]
12. Wang, P.; Wang, J.; Wang, X.; Yu, H.; Yu, J.; Lei, M.; Wang, Y. One-step synthesis of easy-recycling TiO₂-rGO nanocomposite photocatalysts with enhanced photocatalytic activity. *Appl. Catal. B Environ.* **2013**, *132*, 452–459. [[CrossRef](#)]
13. Zhou, W.; Yin, Z.; Du, Y.; Huang, X.; Zeng, Z.; Fan, Z.; Liu, H.; Wang, J.; Zhang, H. Synthesis of few-layer MoS₂ nanosheet-coated TiO₂ nanobelt heterostructures for enhanced photocatalytic activities. *Small* **2013**, *9*, 140–147. [[CrossRef](#)] [[PubMed](#)]
14. Ou, Y.; Lin, J.; Fang, S.; Liao, D. MWNT-TiO₂: Ni composite catalyst: A new class of catalyst for photocatalytic H₂ evolution from water under visible light illumination. *Chem. Phys. Lett.* **2006**, *429*, 199–203. [[CrossRef](#)]
15. Liu, Q.; Huang, J.; Tang, H.; Yu, X.; Shen, J. Construction 0D TiO₂ nanoparticles/2D CoP nanosheets heterojunctions for enhanced photocatalytic H₂ evolution activity. *J. Mater. Sci. Technol.* **2020**, *56*, 196–205. [[CrossRef](#)]
16. Meng, A.; Zhu, B.; Zhong, B.; Zhang, L.; Cheng, B. Direct Z-scheme TiO₂/CdS hierarchical photocatalyst for enhanced photocatalytic H₂-production activity. *Appl. Surf. Sci.* **2017**, *422*, 518–527. [[CrossRef](#)]
17. Cheng, C.; Amini, A.; Zhu, C.; Xu, Z.; Song, H.; Wang, N. Enhanced photocatalytic performance of TiO₂-ZnO hybrid nanostructures. *Sci. Rep.* **2014**, *4*, 4181. [[CrossRef](#)]
18. Yan, J.; Wu, H.; Chen, H.; Zhang, Y.; Zhang, F.; Liu, S.F. Fabrication of TiO₂/C₃N₄ heterostructure for enhanced photocatalytic Z-scheme overall water splitting. *Appl. Catal. B Environ.* **2016**, *191*, 130–137. [[CrossRef](#)]
19. Xie, M.; Fu, X.; Jing, L.; Luan, P.; Feng, Y.; Fu, H. Long-lived, visible-light-excited charge carriers of TiO₂/BiVO₄ nanocomposites and their unexpected photoactivity for water splitting. *Adv. Energy Mater.* **2014**, *4*, 1300995. [[CrossRef](#)]
20. Wang, Y.; Zhu, C.; Zuo, G.; Guo, Y.; Xiao, W.; Dai, Y.; Kong, J.; Xu, X.; Zhou, Y.; Xie, A. 0D/2D Co₃O₄/TiO₂ Z-Scheme heterojunction for boosted photocatalytic degradation and mechanism investigation. *Appl. Catal. B Environ.* **2020**, *278*, 119298. [[CrossRef](#)]
21. Yuan, L.; Weng, B.; Colmenares, J.C.; Sun, Y.; Xu, Y. Multichannel charge transfer and mechanistic insight in metal decorated 2D–2D Bi₂WO₆–TiO₂ cascade with enhanced photocatalytic performance. *Small* **2017**, *13*, 1702253. [[CrossRef](#)] [[PubMed](#)]
22. Zhang, Y.; Xu, J.; Mei, J.; Sarina, S.; Wu, Z.; Liao, T.; Yan, C.; Sun, Z. Strongly interfacial-coupled 2D–2D TiO₂/g-C₃N₄ heterostructure for enhanced visible-light induced synthesis and conversion. *J. Hazard. Mater.* **2020**, *394*, 122529. [[CrossRef](#)] [[PubMed](#)]
23. Liu, Q.; Lu, H.; Shi, Z.; Wu, F.; Guo, J.; Deng, K.; Li, L. 2D ZnIn₂S₄ nanosheet/1D TiO₂ nanorod heterostructure arrays for improved photoelectrochemical water splitting. *ACS Appl. Mater. Interfaces* **2014**, *6*, 17200–17207. [[CrossRef](#)] [[PubMed](#)]
24. Chava, R.K.; Son, N.; Kang, M. Surface engineering of CdS with ternary Bi/Bi₂MoO₆-MoS₂ heterojunctions for enhanced photoexcited charge separation in solar-driven hydrogen evolution reaction. *Appl. Surf. Sci.* **2021**, *565*, 150601. [[CrossRef](#)]
25. Fu, J.; Yu, J.; Jiang, C.; Cheng, B. g-C₃N₄-Based heterostructured photocatalysts. *Adv. Energy Mater.* **2018**, *8*, 1701503. [[CrossRef](#)]
26. Wen, J.; Xie, J.; Chen, X.; Li, X. A review on g-C₃N₄-based photocatalysts. *Appl. Surf. Sci.* **2017**, *391*, 72–123. [[CrossRef](#)]

27. Chava, R.K.; Do, J.; Kang, M. Strategy for improving the visible photocatalytic H₂ evolution activity of 2D graphitic carbon nitride nanosheets through the modification with metal and metal oxide nanocomponents. *Appl. Catal. B Environ.* **2019**, *248*, 538–551. [[CrossRef](#)]
28. Ran, Y.; Cui, Y.; Zhang, Y.; Fang, Y.; Zhang, W.; Yu, X.; Lan, H.; An, X. Assembly-synthesis of puff pastry-like g-C₃N₄/CdS heterostructure as S-junctions for efficient photocatalytic water splitting. *Chem. Eng. J.* **2022**, *431*, 133348. [[CrossRef](#)]
29. Cabot, A.; Du, R.; Xiao, K.; Li, B.; Han, X.; Zhang, C.; Wang, X.; Zuo, Y.; Pablo, G.; Li, J.; et al. Controlled Oxygen Doping in Highly Dispersed Ni-Loaded G-C₃N₄ Nanotubes for Efficient Photocatalytic H₂O₂ Production. *SSRN Electron. J.* **2022**, *441*, 135999. [[CrossRef](#)]
30. Zhang, X.; Yuan, X.; Jiang, L.; Zhang, J.; Yu, H.; Wang, H.; Zeng, G. Powerful combination of 2D g-C₃N₄ and 2D nanomaterials for photocatalysis: Recent advances. *Chem. Eng. J.* **2020**, *390*, 124475. [[CrossRef](#)]
31. Zuo, Y.; Xu, X.; Zhang, C.; Li, J.; Du, R.; Wang, X.; Han, X.; Arbiol, J.; Llorca, J.; Liu, J.; et al. SnS₂/g-C₃N₄/graphite nanocomposites as durable lithium-ion battery anode with high pseudocapacitance contribution. *Electrochim. Acta* **2020**, *349*, 136369. [[CrossRef](#)]
32. Fu, J.; Xu, Q.; Low, J.; Jiang, C.; Yu, J. Ultrathin 2D/2D WO₃/g-C₃N₄ step-scheme H₂-production photocatalyst. *Appl. Catal. B Environ.* **2019**, *243*, 556–565. [[CrossRef](#)]
33. Qin, Y.; Li, H.; Lu, J.; Feng, Y.; Meng, F.; Ma, C.; Yan, Y.; Meng, M. Synergy between van der waals heterojunction and vacancy in ZnIn₂S₄/g-C₃N₄ 2D/2D photocatalysts for enhanced photocatalytic hydrogen evolution. *Appl. Catal. B Environ.* **2020**, *277*, 119254. [[CrossRef](#)]
34. Cao, S.; Shen, B.; Tong, T.; Fu, J.; Yu, J. 2D/2D heterojunction of ultrathin MXene/Bi₂WO₆ nanosheets for improved photocatalytic CO₂ reduction. *Adv. Funct. Mater.* **2018**, *28*, 1800136. [[CrossRef](#)]
35. Su, J.; Li, G.; Li, X.; Chen, J. 2D/2D heterojunctions for catalysis. *Adv. Sci.* **2019**, *6*, 1801702. [[CrossRef](#)]
36. Urbain, F.; Du, R.; Tang, P.; Smirnov, V.; Andreu, T.; Finger, F.; Divins, N.J.; Llorca, J.; Arbiol, J.; Cabot, A. Upscaling high activity oxygen evolution catalysts based on CoFe₂O₄ nanoparticles supported on nickel foam for power-to-gas electrochemical conversion with energy efficiencies above 80%. *Appl. Catal. B Environ.* **2019**, *259*, 118055. [[CrossRef](#)]
37. Zuo, Y.; Liu, Y.; Li, J.; Du, R.; Yu, X.; Xing, C.; Zhang, T.; Yao, L.; Arbiol, J.; Llorca, J. Solution-processed ultrathin SnS₂-Pt nanoplates for photoelectrochemical water oxidation. *ACS Appl. Mater. Interfaces* **2019**, *11*, 6918–6926. [[CrossRef](#)]
38. Zhang, C.; Du, R.; Biendicho, J.J.; Yi, M.; Xiao, K.; Yang, D.; Zhang, T.; Wang, X.; Arbiol, J.; Llorca, J.; et al. Tubular CoFeP@CN as a Mott-Schottky Catalyst with Multiple Adsorption Sites for Robust Lithium–Sulfur Batteries. *Adv. Energy Mater.* **2021**, *11*, 2100432. [[CrossRef](#)]
39. Liu, M.; Piao, L.; Lu, W.; Ju, S.; Zhao, L.; Zhou, C.; Li, H.; Wang, W. Flower-like TiO₂ nanostructures with exposed {001} facets: Facile synthesis and enhanced photocatalysis. *Nanoscale* **2010**, *2*, 1115–1117. [[CrossRef](#)]
40. Li, Y.; Lv, K.; Ho, W.; Dong, F.; Wu, X.; Xia, Y. Hybridization of rutile TiO₂ (rTiO₂) with g-C₃N₄ quantum dots (CN QDs): An efficient visible-light-driven Z-scheme hybridized photocatalyst. *Appl. Catal. B Environ.* **2017**, *202*, 611–619. [[CrossRef](#)]
41. Tian, N.; Zhang, Y.; Li, X.; Xiao, K.; Du, X.; Dong, F.; Waterhouse, G.I.N.; Zhang, T.; Huang, H. Precursor-reforming protocol to 3D mesoporous g-C₃N₄ established by ultrathin self-doped nanosheets for superior hydrogen evolution. *Nano Energy* **2017**, *38*, 72–81. [[CrossRef](#)]
42. Tian, N.; Huang, H.; Wang, S.; Zhang, T.; Du, X.; Zhang, Y. Facet-charge-induced coupling dependent interfacial photocharge separation: A case of BiOI/g-C₃N₄ pn junction. *Appl. Catal. B Environ.* **2020**, *267*, 118697. [[CrossRef](#)]
43. Yu, X.; Du, R.; Li, B.; Zhang, Y.; Liu, H.; Qu, J.; An, X. Biomolecule-assisted self-assembly of CdS/MoS₂/graphene hollow spheres as high-efficiency photocatalysts for hydrogen evolution without noble metals. *Appl. Catal. B Environ.* **2016**, *182*, 504–512. [[CrossRef](#)]
44. Du, R.; Zhang, Y.; Li, B.; Yu, X.; Liu, H.; An, X.; Qu, J. Biomolecule-assisted synthesis of defect-mediated Cd_{1-x}Zn_xS/MoS₂/graphene hollow spheres for highly efficient hydrogen evolution. *Phys. Chem. Chem. Phys.* **2016**, *18*, 16208–16215. [[CrossRef](#)] [[PubMed](#)]
45. Chen, Y.; Liu, X.; Hou, L.; Guo, X.; Fu, R.; Sun, J. Construction of covalent bonding oxygen-doped carbon nitride/graphitic carbon nitride Z-scheme heterojunction for enhanced visible-light-driven H₂ evolution. *Chem. Eng. J.* **2020**, *383*, 123132. [[CrossRef](#)]